Analysis of Terahertz Surface Emitting Quantum-Cascade Lasers

Martin Schubert, *Student Member, IEEE,* and Farhan Rana, *Member, IEEE*

***Abstract*—An analysis of surface-emitting terahertz quantum-cascade lasers operating at wavelengths near 100 μm is presented. The devices use distributed feedback through second-order Bragg metal gratings to generate strong emission of radiation normal to the laser surface. The analysis is based on coupling between the exact Floquet–Bloch eigenmodes of infinite periodic structures in finite length devices. The results show performance of surface-emitting terahertz lasers comparable to edge-emitting devices, with high radiative efficiencies and low threshold gains. Using phase-shifts in the grating, high-quality single-lobe beams in the farfield are obtained.**

***Index Terms*—Coupling coefficients, distributed feedback (DFB) lasers, Floquet–Bloch expansion, quantum-cascade laser, surface emission.**

I. Introduction

TERAHERTZ quantum-cascade lasers are emerging as important sources of coherent terahertz radiation with applications such as screening for weapons, explosives, and biohazards, imaging concealed objects, medical imaging, environment control and pollution monitoring, spectroscopy, remote sensing and surveillance, and ultrabroad-band communications [1]–[7]. Research on terahertz quantum-cascade lasers to this point has primarily focused on edge-emitting lasers. These devices typically use active regions capped by metal and grown on insulating substrates [8]–[12], or active regions surrounded by metal on both sides [13]–[16]. The double-metal waveguide structure can achieve an overlap with the active region close to unity [13] and has high reflectivity [17], resulting in low threshold gains. However, this design confines the transverse optical mode in regions with spatial dimensions up to ten times smaller than the wavelength. This extreme confinement results in strong diffraction of the output beam and broad output beam widths.

Surface emitting quantum-cascade lasers using second-order gratings have been realized in the mid-infrared (mid-IR) region ($\sim$ 10 μm wavelength) [18]–[20]. This paper shows that surface-emitting terahertz quantum-cascade lasers ($\sim$ 100 μm wavelength) can be designed to have radiative efficiencies nearly as good as edge emitters while maintaining comparable threshold gains. Mid-IR surface-emitting quantum-cascade lasers reported in [19] and [20] had a double lobe farfield pattern with a null in the center. Recently, phase-shifted second-order gratings have been used to obtain single lobe farfield patterns in surface-emitting near-IR interband lasers [21]–[23]. Our results show that phase-shifted metallic second-order gratings can also be used in terahertz lasers to obtain single lobe farfield beam patterns with narrow beam widths without sacrificing performance.

The conventional coupled-mode theory for optical waveguides with TE-polarized light and first-order gratings is not applicable to devices with TM-polarized light and strong second-order metal gratings [24]. To study surface-emitting terahertz quantum-cascade lasers, this work uses a numerical scheme that is based on the exact Floquet–Bloch eigenmodes of infinitely long periodic laser structures. Perfectly matched layer (PML) boundary conditions are implemented in the numerical scheme to compute the outgoing radiation [25]. The field in finite length devices is then described in terms of the infinite length eigenmodes using a novel coupled-mode theory. This approach enables accurate simulation of second-order gratings with very strong index contrast.

This paper is organized as follows. Section II describes the basic structure of surface-emitting lasers investigated in this paper. Section III describes the simulation technique used, including the Floquet–Bloch analysis and the resulting coupled-mode theory. Section IV presents the performance of surface-emitting terahertz lasers as a function of various device parameters. Section V treats the farfield radiation pattern produced by surface-emitting lasers. Section VI gives concluding remarks.

II. Laser Structure

Fig. 1 shows the basic structure of the surface-emitting lasers considered in this paper. The structure consists of an approximately 10-μm-thick quantum-cascade active region surrounded by n$^+$ contact and gold layers. The gold layers serve to tightly confine the optical mode to the active region. This waveguide design is similar to the one used previously for an edge emitting device in [9]. The active region contains n-doped quantum wells which yield an average carrier density of 4.56×10^{15} cm^{-3} for the entire active region. Below the active region is a 200-nm-thick n$^+$ contact layer doped at 2×10^{18} cm^{-3}. The bottom gold layer is 2 μm thick. The top contact layer is doped at 5×10^{18} cm^{-3} and is 60 nm thick. The top gold layer is 1 μm thick. Both the top contact and gold layer are patterned to form the second-order grating. Simulations included a 25-μm-thick region of air above the grating. Since the skin-depth of gold at terahertz frequencies is less than 0.1 μm, the thickness of the bottom gold layer is sufficient for all guided and radiated modes to decay completely. Above the air region, a PML absorbing

Manuscript received September 27, 2005; revised November 11, 2005. This work was supported in part by the National Science Foundation (NSF), in part by NASA, in part by Infotonics Inc., in part by NPACI Supercomputer Center, and in part by Intel.

The authors are with Cornell University, Ithaca, NY 14853 USA (e-mail: mfs24@cornell.edu).

Digital Object Identifier 10.1109/JQE.2005.863138

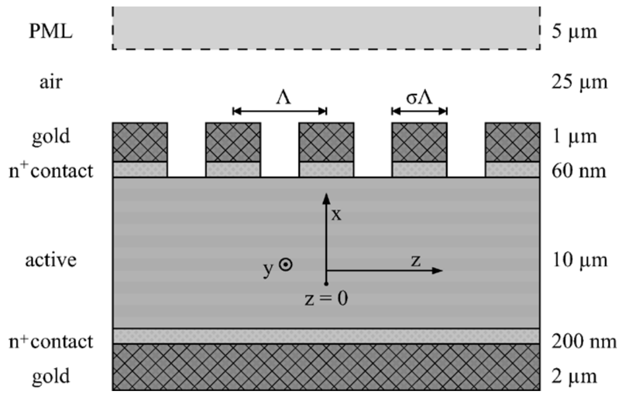

Fig. 1. Laser structure under consideration. The grating has periodicity Λ and duty cycle σ.

boundary layer is used to accurately calculate the outgoing radiation.

The dielectric constants of the different materials in the laser structure were calculated using the Drude model [26], with scattering times of $\tau = 0.5$ ps and $\tau = 0.1$ ps for the lightly doped and heavily doped semiconductor regions, respectively. A scattering time of $\tau = 0.05$ ps was used for the gold [8], [9].

Strong interaction between the field and the grating causes the wavelengths that are resonant in the structure to act as strong functions of the grating duty cycle σ. In the analysis presented here, the free-space wavelength of the lasing modes is kept close to 100 μm when the grating duty cycle is varied by slightly adjusting the grating period. Specifically, the period is decreased almost linearly from 37.6 to 28.2 μm as σ is swept from 0 to 1.

III. Solution Technique

A. Floquet–Bloch Solutions for the Infinite Length Structure

The analysis of surface-emitting lasers uses the exact eigenmodes of an infinite length device as the basis for expanding the modes of a finite length device. We consider only TM-polarized modes where the magnetic field is polarized in the y-direction (see Fig. 1). The electric field can be polarized in either the x- or z-direction. The displacement flux density is related to the electric field as

$$\vec{D} = \begin{bmatrix} \varepsilon_x & 0 \\ 0 & \varepsilon_z \end{bmatrix} \begin{bmatrix} E_x \\ E_z \end{bmatrix}. \tag{1}$$

Here, the imaginary parts of the dielectric constants include the effects of the material loss as well as the material gain. ε_x and ε_z differ because only the x-component of the electric field experiences gain. Adding gain to the structure involves a perturbation to ε_x given by $\Delta\varepsilon_x = -ig\Re(n_{\mathrm{act}}\lambda)/2\pi$, where g is the material gain, n_{act} is the index of refraction of the active region, and λ is the free space wavelength of the lasing mode.

The magnetic field in the structure is governed by the wave equation

$$\frac{\partial}{\partial x}\left[\frac{1}{\varepsilon_z}\frac{\partial H}{\partial x}\right] + \frac{\partial}{\partial z}\left[\frac{1}{\varepsilon_x}\frac{\partial H}{\partial z}\right] = -k^2 H. \tag{2}$$

Because of the periodic nature of the structure, the inverse complex dielectric function can be expanded in a Fourier series as

$$\frac{1}{\varepsilon_x(x,z)} = v_x(x,z) = \sum_{m=-\infty}^{+\infty} v_{m,x}(x) e^{im\beta_0 z}. \tag{3}$$

A similar expansion is used for $1/\varepsilon_z$. Here, $\beta_0 = 2\pi/\Lambda$ is the grating vector. In the infinite length device, the field inside the device must have the same periodicity as the grating, and can be written exactly as a Floquet–Bloch expansion

$$H(x,z) = \sum_{m=-\infty}^{+\infty} H_m(x) e^{im\beta_0 z}. \tag{4}$$

In this expression, surface normal radiation is described by the zeroth-order component H_0. By plugging the above expansions into (2), the Floquet–Bloch components of the magnetic field are found to satisfy the complex eigenvalue equation

$$\sum_{p=-\infty}^{+\infty}\left[\frac{\partial}{\partial x}\left[v_{m-p,z}\frac{\partial H_p}{\partial x}\right] - mp\beta_0^2 v_{m-p,x} H_p\right] = -k^2 H_m. \tag{5}$$

The above equation is solved by the finite difference technique using a truncated set of field components in the Floquet–Bloch expansion. A perfectly matched absorbing boundary layer is used to satisfy the outgoing radiation boundary condition [25].

Solution of (5) yields two orthogonal eigenmodes $H^s(x,z)$ and $H^a(x,z)$ with field patterns that are symmetric and antisymmetric with respect to the grating. These modes are normalized as

$$\sum_m \int_{-\infty}^{\infty} \left(H_m^{\frac{s}{a}}(x)\right)^2 dx = 1 \tag{6}$$

and obey the orthogonality condition

$$\sum_m \int_{-\infty}^{\infty} H_m^a(x) H_m^s(x) dx = 0. \tag{7}$$

The symmetric and antisymmetric modes have k-values k_s and k_a, respectively, where the real part is the free-space propagation constant and the imaginary part corresponds to net modal loss (or net modal gain). Fig. 2 shows the convergence of the computed k-values as function of the maximum number of plane wave components included in the Floquet–Bloch expansion. Good convergence is obtained by including more than 20 plane wave components in the Floquet–Bloch expansion.

Figs. 3 and 4 show the numerically calculated magnetic and electric fields for the symmetric and antisymmetric eigenmodes. In the symmetric mode, the forward- and backward-going plane waves are in phase ($H_m^s = H_{-m}^s$), while they are out of phase for the antisymmetric mode ($H_m^a = -H_{-m}^a$). These phase relationships are responsible for shaping the field patterns shown in Figs. 3 and 4. In the antisymmetric mode, lobes of opposite sign for the magnetic and z-polarized electric fields appear between the grating teeth. The field interferes destructively outside the grating, and the radiating component H_0^a is zero. The symmetric mode is the one which radiates, and has a nonzero radiating component H_0^s. Consequently, the symmetric mode has

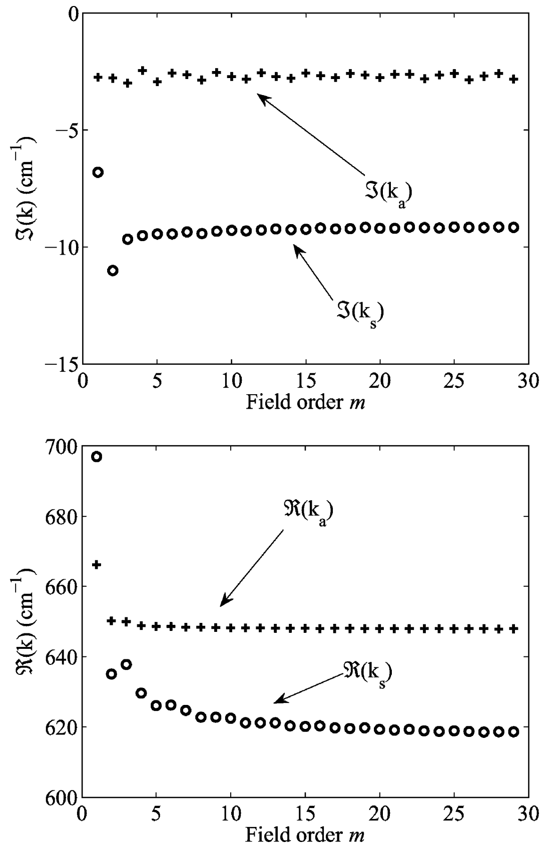

Fig. 2. Convergence of the real and imaginary parts of the k-vectors for the symmetric (k_s) and the antisymmetric (k_a) modes as a function of the maximum number of plane wave components used in the Floquet–Bloch expansion. The duty cycle σ of the grating is 0.7.

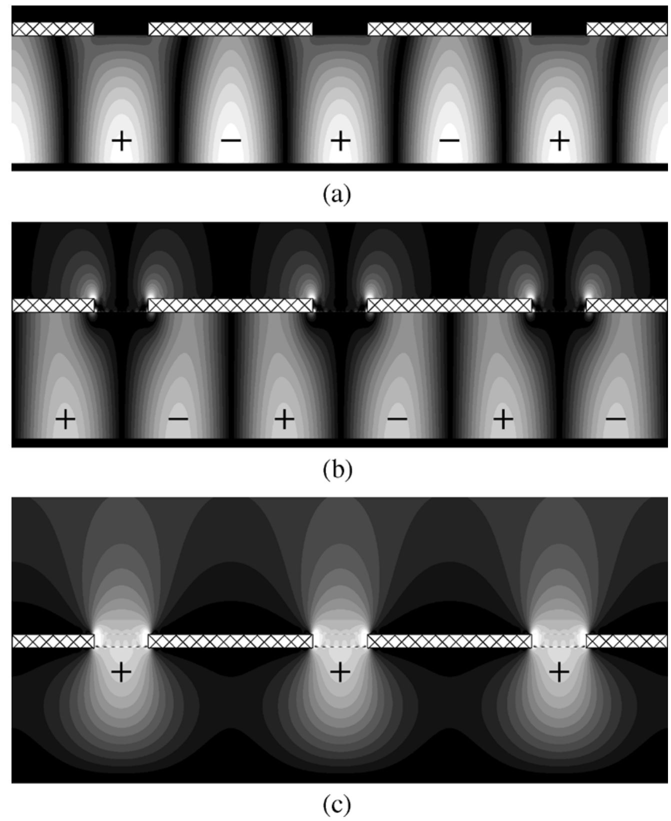

Fig. 3. Magnitude of the (a) magnetic field, (b) x-polarized component, and (c) z-polarized component of the electric field for the symmetric mode for $\sigma = 0.75$.

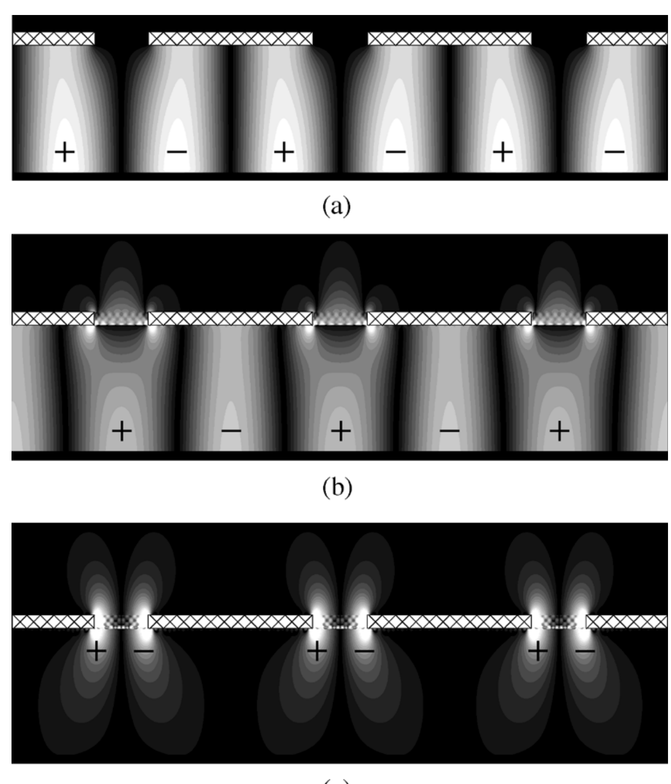

Fig. 4. Magnitude of the (a) magnetic field, (b) x-polarized component, and (c) z-polarized component of the electric field for the antisymmetric mode for $\sigma = 0.75$.

higher threshold gain, and the antisymmetric mode is the lasing mode for an infinite length device.

B. Coupled-Mode Theory for the Finite Length Structure

The field in a finite length laser is expressed as a linear superposition of the two modes of an infinite length structure

$$H(x, z) = B^s(z)H^s(x, z) + B^a(z)H^a(x, z) \tag{8}$$

where B^s and B^a are slowly varying mode amplitudes. This technique is similar to the $\mathbf{k} \cdot \mathbf{p}$ method that is used to find the electronic band structure near the band edges in semiconductor heterostructures [27]. Plugging the expansion in (8) in (2) and using (5)–(7), B^a and B^s are found to satisfy the coupled-mode equation

$$\frac{\partial}{\partial z}\begin{bmatrix} B^s(z) \\ B^a(z) \end{bmatrix} = \begin{bmatrix} 0 & i\zeta - i\kappa \\ i\zeta + i\kappa & 0 \end{bmatrix}\begin{bmatrix} B^s(z) \\ B^a(z) \end{bmatrix} \tag{9}$$

where ζ and κ are given by

$$\zeta = \frac{1}{2f\beta_0}\left(2k_0^2 - k_s^2 - k_a^2\right) \tag{10}$$

$$\kappa = \frac{1}{2f\beta_0}\left(k_a^2 - k_s^2\right) \tag{11}$$

and the term f is calculated as

$$f = \sum_{m,p}(m - p)\int_{-\infty}^{\infty} H_m^s(x)H_p^a(x)v_{-m-p,x}(x)dx. \tag{12}$$

Here, k_0 equals $2\pi/\lambda_o$ where λ_o is the free-space wavelength of the lasing mode. Gain is included in (9) by using gain dependent values for k_s, k_a, and f.

The coupled-mode theory presented here is different from the conventional coupled-mode theory where coupling takes place between forward- and backward-propagating modes [24], [28], [29]. Here, coupling takes place between the symmetric and antisymmetric eigenmodes of the infinite length structure. The connection with traditional coupled-mode theory is made in Appendix I, where it is shown that the coupling between the forward- and backward-propagating modes is described by κ. The splitting between k_s and k_a, given by κ, is proportional to the second harmonic of the grating which couples forward- and backward-going plane waves through Bragg reflection.

C. Boundary Conditions

In an infinite length device, only the antisymmetric mode lases because it does not radiate and experiences less loss. In a finite length device, highly reflecting metal facet coatings can be used to eliminate the antisymmetric component at the two ends of the device and maximize the radiating symmetric component. This can be achieved by placing the highly reflecting facets at locations z that are multiples of $\Lambda/2$ (where the location $z=0$ is in the center of the device and the middle of a grating tooth, as shown in Fig. 1). At these locations, the forward- and backward-going plane waves of the magnetic field for the symmetric mode are in phase, which satisfies the boundary condition of a metallic reflector. At the same locations, the plane waves are out of phase for the antisymmetric mode, which forces the following boundary condition at the two facets

$$B^a\left(-\frac{L}{2}\right) = B^a\left(\frac{L}{2}\right) = 0. \tag{13}$$

D. Solutions

The coupled equations in (9) can be solved to find the lasing wavelength and threshold material gain for the finite length device. The solution takes the form

$$B^s(z) = b^s \cos\left(\sqrt{\zeta^2-\kappa^2}\left(z+\frac{L}{2}\right)\right) \tag{14}$$

$$B^a(z) = b^a \sin\left(\sqrt{\zeta^2-\kappa^2}\left(z+\frac{L}{2}\right)\right). \tag{15}$$

The boundary condition (13) will hold provided

$$\sqrt{\zeta^2-\kappa^2}L = n\pi \qquad n=1,2,3,\ldots \tag{16}$$

The different values of n correspond to the longitudinal modes of the laser. For each n, there are two sets of k_0 and g which satisfy (9)—one solution on either side of the gap between k_s and k_a. The longitudinal mode spectrum of a typical device is discussed in Section IV.

The lowest threshold gain occurs for $n=1$ with k_0 close to k_a. Fig. 5 shows the squared magnitudes of the calculated symmetric and antisymmetric envelopes, $|B^s(z)|^2$ and $|B^a(z)|^2$ respectively, for the lasing mode in a finite length device. The facet boundary conditions force the antisymmetric component to be zero at the edges. Coupling between the modes transfers the energy from the symmetric component to the antisymmetric component away from the edges of the device.

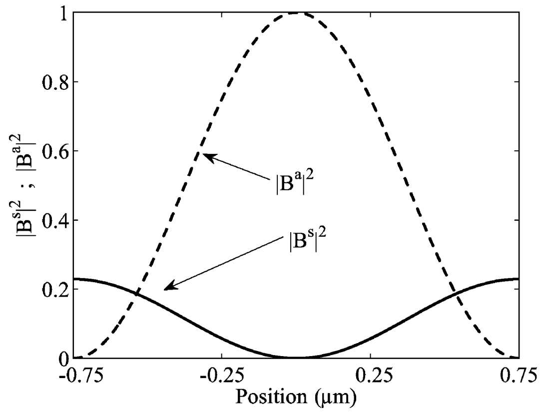

Fig. 5. Symmetric and antisymmetric parts, $|B^s(z)|^2$ and $|B^a(z)|^2$, respectively, of the lasing mode for a 1.5-mm-long laser device with a grating duty cycle of 0.6. The boundary conditions force the lasing mode to be completely symmetric at the edges, but coupling transforms it to purely antisymmetric in the center of the device.

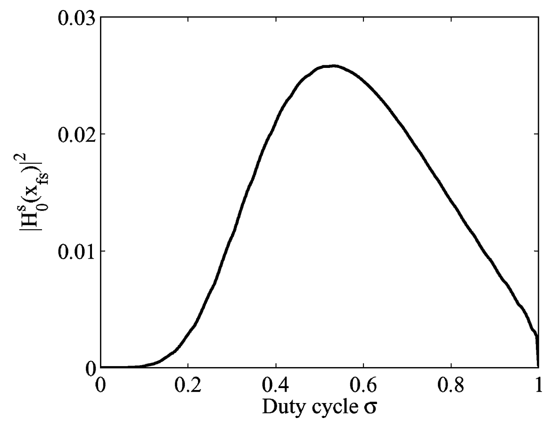

Fig. 6. Square-magnitude $|H_0^s(x_{fs})|^2$ of the radiating plane wave component of the symmetric mode, normalized to the maximum square-magnitude of the field inside the waveguide, plotted as a function of the grating duty cycle σ. The location x_{fs} corresponds to a point just above the grating in free space.

IV. Results and Discussion

The device performance is characterized by the radiative efficiency and the threshold gain, and is determined by the grating duty cycle σ, grating coupling strength, and the device length. Below, we examine the effect of various device parameters on device performance.

A. Radiation Field Amplitude

The radiative efficiency is proportional to the amplitude of the radiating plane wave component H_0^s in the Floquet–Bloch expansion of the symmetric mode. Fig. 6 shows $|H_0^s(x_{fs})|^2$ plotted as a function of the grating duty cycle σ and normalized to the maximum square-magnitude of the field inside the waveguide. The location x_{fs} corresponds to a point in free space just above the grating. Since the magnitude of the radiating plane wave component is proportional to the first harmonic of the grating, Fig. 6 shows a maximum near $\sigma=0.5$.

B. Symmetric and Antisymmetric Parts of the Lasing Mode

Because only the symmetric mode radiates, the radiative efficiency of the laser is proportional to the total energy in the sym-

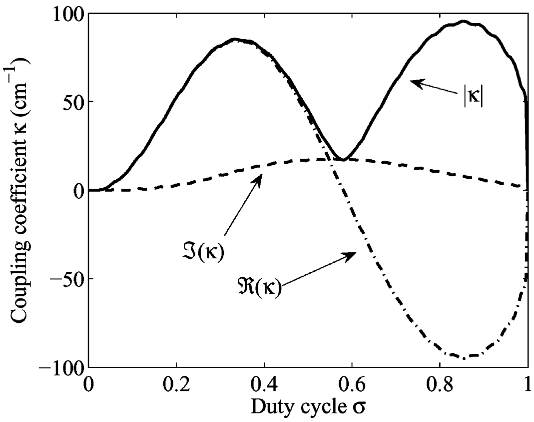

Fig. 7. κ plotted as a function of the grating duty cycle σ.

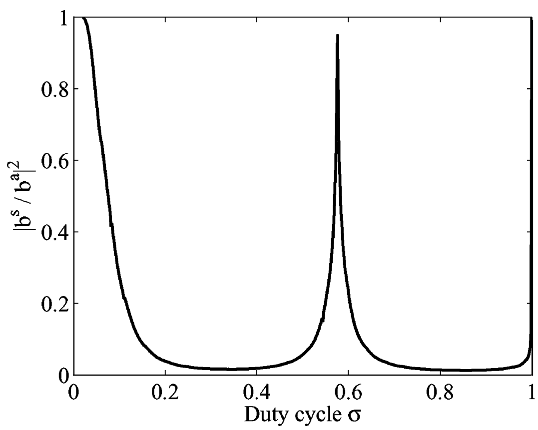

Fig. 8. Ratio of the energies in the symmetric and antisymmetric parts of the lasing mode plotted as a function of the grating duty cycle in a 1.5-mm-long device.

metric part of the lasing mode. The ratio of the energies in the symmetric and antisymmetric parts of the lasing mode is given by

$$\left|\frac{b^s}{b^a}\right|^2 = \left|\frac{\zeta-\kappa}{\zeta+\kappa}\right| = \left|\frac{1}{\zeta+\kappa}\right|^2\left(\frac{\pi}{L}\right)^2 \tag{17}$$

Equation (17) shows that as the device length increases, the symmetric fraction will decrease. This agrees with the fact that the antisymmetric mode is the lasing mode for an infinite length device.

For the device lengths considered in this paper $(L > 1\ \text{mm})$, the lasing mode is dominated by the antisymmetric mode. As a result, the value of k_0 is typically very close to that of k_a, and, $\zeta + \kappa \sim 2\kappa$. Therefore, from (17), the fraction of the symmetric component in the lasing mode is inversely proportional to the value of $|\kappa|$. Fig. 7 shows the behavior of κ as a function of the grating duty cycle σ. As expected, κ has a minimum near $\sigma = 0.5$, where the second harmonic of the grating is minimized. The gold grating at terahertz frequencies is a significant perturbation to the waveguide. As a result, $|\kappa|$ reaches values as high as 100 cm^{-1}. Fig. 8 shows the ratio of the energies in the symmetric and antisymmetric parts of the lasing mode as a function of the grating duty cycle. Together with Fig. 7, Fig. 8 demonstrates the relationship between κ and the ratio of energies in the symmetric and antisymmetric eigenmodes.

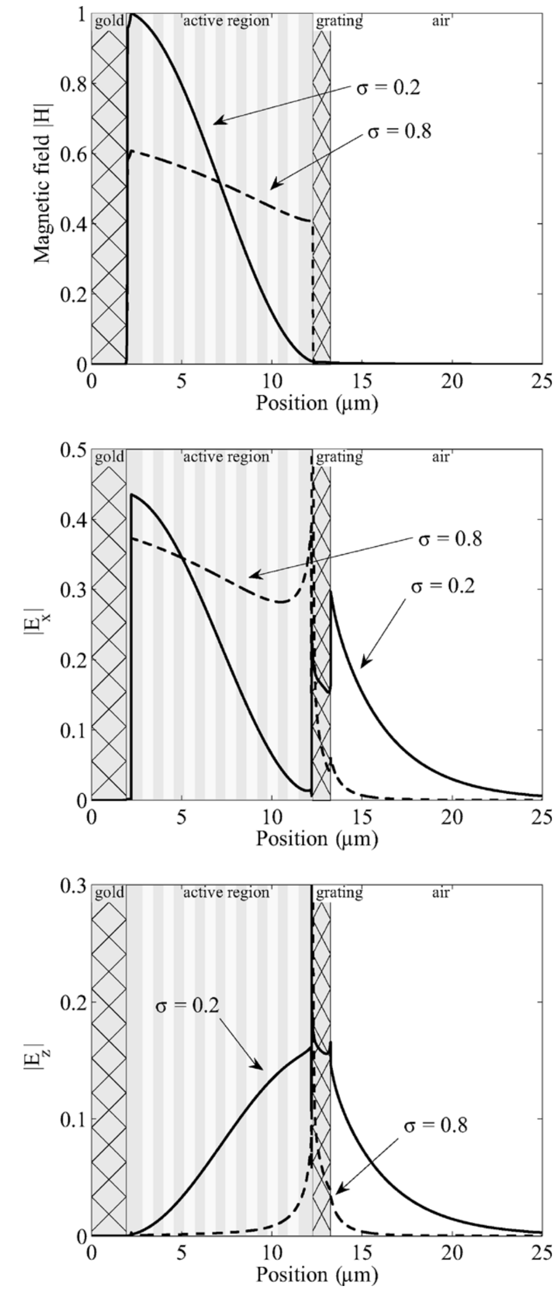

Fig. 9. Magnitude of the modal magnetic field and x and z components of the modal electric field for the antisymmetric mode integrated along z for one period. Fields for $\sigma = 0.2$ and $\sigma = 0.8$ are shown.

C. Electric Field Polarization

The presence of a metal grating results in significant changes in the relative proportions of the x and z components of the modal electric field as a function of the grating duty cycle. The field profiles for duty cycles of 0.2 and 0.8 are shown in Fig. 9. Electric fields are computed directly from the full magnetic fields with all plane wave components. Fig. 9 shows that for small duty cycles, the z-polarized electric field is large in magnitude. In addition, for small duty cycles the electric field leaks out through the grating gaps.

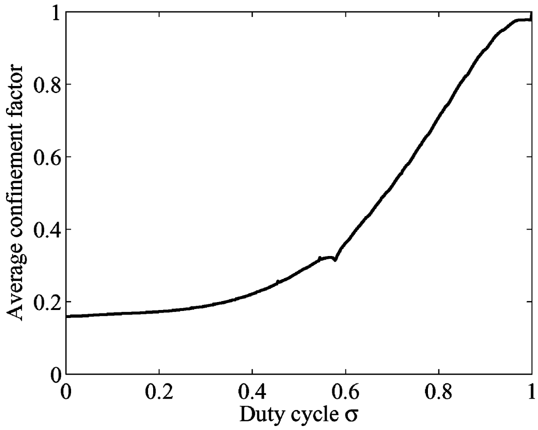

Fig. 10. Average confinement factor Γ for the x-polarized electric field for a 1.5-mm device. The dip in the center coincides with a minimum in κ.

Fig. 10 shows the confinement factor of the x-component of the modal electric field averaged along the length of the device. The confinement factor is calculated as

$$\Gamma = \frac{\int_0^L \int_{\text{active}} |E_x|^2 dxdz}{\int_0^L \int |E_x|^2 + |E_z|^2 dxdz}. \tag{18}$$

In (18), the radiating component of E_z is neglected outside the waveguide. For a duty cycle of 1, the field is polarized almost entirely in the x direction, and the overlap is close to unity. As the duty cycle is reduced from unity, the z-component of the electric field increases in magnitude, and the electric field leaks out of the active region. These factors combine to reduce the confinement factor, and result in increased threshold gain at low duty cycles. This is discussed in greater detail in the next section.

D. Threshold Gain and Radiative Efficiency

The radiative efficiency η_{surf} of the laser is determined by the ratio of power radiated from the surface to the total power generated through stimulated emission in the active region. The radiated power is obtained by integrating the Poynting vector of the radiation field over the length of the device and is given by

$$P_{\text{surf}} = \frac{1}{2}\sqrt{\frac{\mu_0}{\varepsilon_0}}\,|H_0^s(x_{fs})|^2 \int_0^L |B^s|^2 dz. \tag{19}$$

The total power generated through stimulated emission in the waveguide is given by

$$P_{stim} = \frac{\varepsilon_0 n_{\text{act}} c}{2} g_{\text{th}} \int_0^L \int_{\text{active}} |E_x(x,z)|^2\, dxdz. \tag{20}$$

Here, g_{th} is the threshold gain, and the integration in x is over the active region only.

The threshold gain of the laser and the radiative efficiency are shown in Fig. 11 as a function of the grating duty cycle σ for a 1.5 mm device. Also shown is the achievable performance for a double-metal waveguide edge emitting laser with identical laser structure and typical facet reflectivity values between 0.6 and 0.9 [17]. For the surface emitter, both the threshold gain and the external efficiency are characterized by a large peak near $\sigma =$ 0.56. These peaks coincide with the grating duty cycle where both the radiating amplitude $|H_0^s(x_{fs})|^2$ and the fraction of the lasing mode which is symmetric are large, as shown earlier in Figs. 6 and 8. Fig. 12 explicitly shows the radiative loss and the waveguide loss for a 1.5 mm long device, calculated as $\alpha_{\text{surf}} = g_{\text{th}}\Gamma\eta_{\text{surf}}$ and $\alpha_{wg} = g_{\text{th}}\Gamma(1-\eta_{\text{surf}})$. While the waveguide loss decreases for small duty cycles, the threshold gain actually

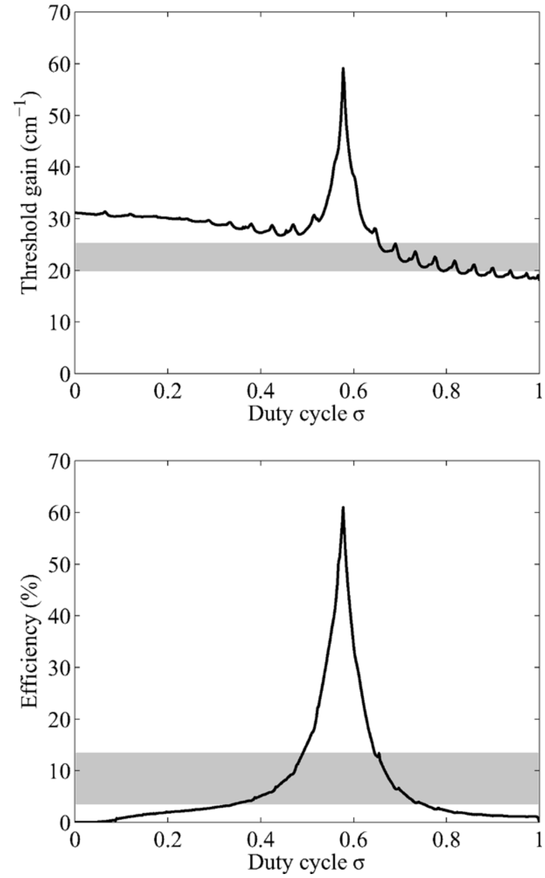

Fig. 11. Threshold gain and outcoupling efficiency are plotted as a function of the grating duty cycle σ for a 1.5-mm-long device. The shaded region shows the threshold gain and single-facet extraction efficiency for a 1.5-mm edge-emitting laser with facet reflectivity ranging from 0.6 to 0.9. Much higher efficiency as achievable with the surface-emitting design.

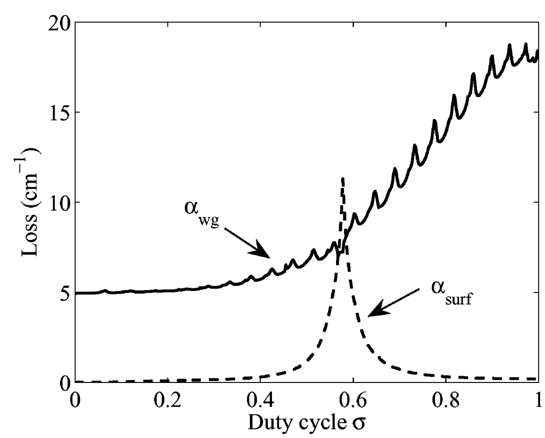

Fig. 12. Radiative loss and waveguide loss as a function of duty cycle for a 1.5-mm-long device.

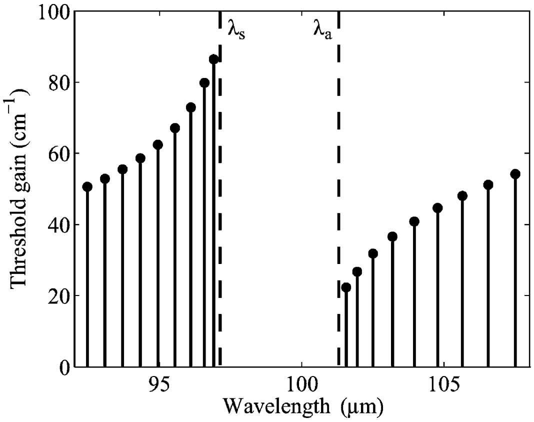

Fig. 13. Longitudinal mode spectrum for a 1.5-mm device with $\sigma = 0.7$. The dashed lines indicate the lasing wavelengths λ_s and λ_a for the infinite length eigenmodes H_s and H_a.

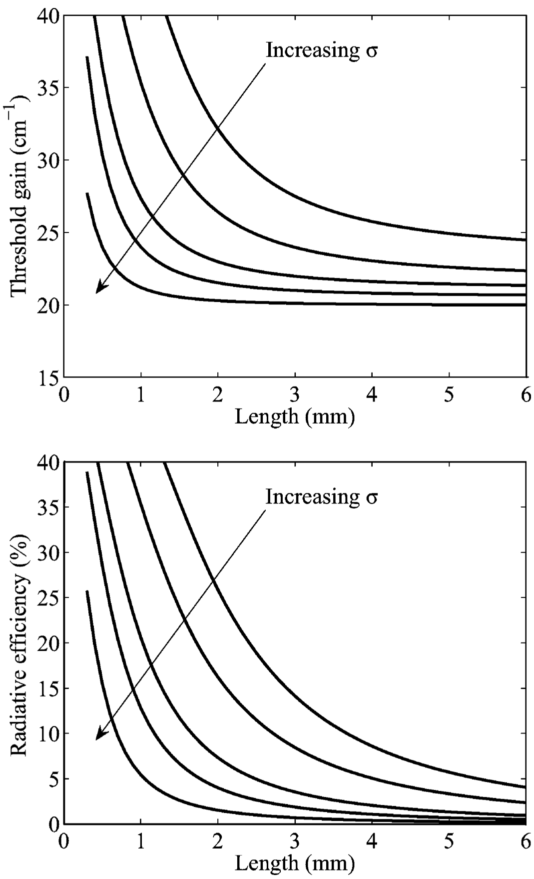

Fig. 14. Threshold gain and radiation outcoupling efficiency as a function of length for devices with various duty cycles. (σ =0.6, 0.62, 0.66, 0.70, 0.80).

increases. This is due to the fact that the confinement factor of the x-polarized electric field decreases for small grating duty cycles, as seen in Fig. 10. The periodic peaks observed in the plot of waveguide loss are the result of field resonances in the grating region.

Fig. 13 plots the calculated threshold gain and emission wavelength for the longitudinal mode spectrum of a 1.5-mm device with a duty cycle σ of 0.7. The threshold gain for the lasing mode is 22.3 cm^{-1}, and the intermodal gain discrimination is 4.2 cm^{-1}.

Fig. 14 shows the radiative efficiency and threshold gain plotted as a function of device length for several different grating duty cycles. As the laser length increases, the symmetric fraction of the lasing mode decreases, resulting in lower radiative efficiency. As expected, the radiative efficiency tends toward zero as the device length increases, while the radiative loss and threshold gain decrease. For very long device lengths, the threshold gain is determined completely by the material losses.

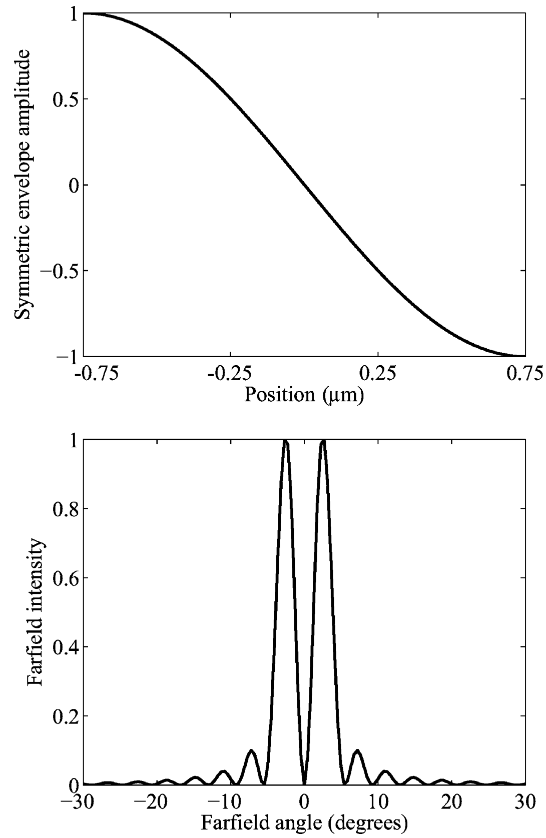

Fig. 15. Amplitude $B^s(z)$ of the symmetric component of the lasing mode and the far-field intensity pattern are plotted. The device length is 1.5 mm and $\sigma = 0.6$. The antisymmetric nearfield pattern produces a null in the far-field in the direction normal to the laser surface.

V. Far-Field Performance

The far-field radiation pattern is related to the near-field pattern by the expression [30]

$$G(\theta) = \frac{\left|\sin(\theta)\int_0^L B^s(z)e^{ik_0\sin(\theta)z}dz\right|^2}{\int_0^{\frac{\pi}{2}}\left|\sin(\theta)\int_0^L B^s(z)e^{ik_0\sin(\theta)z}dz\right|^2\sin(\theta)d\theta}. \quad (21)$$

Fig. 15 shows the amplitude B^s of the symmetric component and the far-field radiation pattern for the lasing mode in a 1.5-mm-long device. B^s has equal magnitude but opposite sign at the two edges of the device. The radiation from each half of the device adds destructively in the direction normal to the laser surface resulting in a null in the center of the far-field radiation pattern. A single-lobed far-field radiation pattern can be obtained by adding a π phase shift in the center of the grating [21]–[23]. The π phase shift is added by extending a metal tooth in the grating by $\Lambda/2$. Adding a π phase shift has

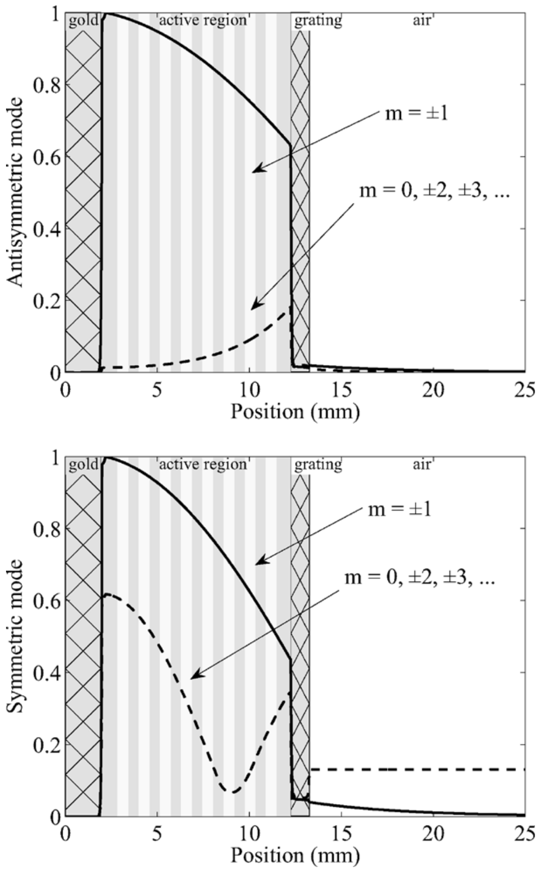

Fig. 16. Magnitude of the first and higher order magnetic field plane wave components for the symmetric and antisymmetric modes integrated along z underneath a grating tooth. The duty cycle σ is 0.7.

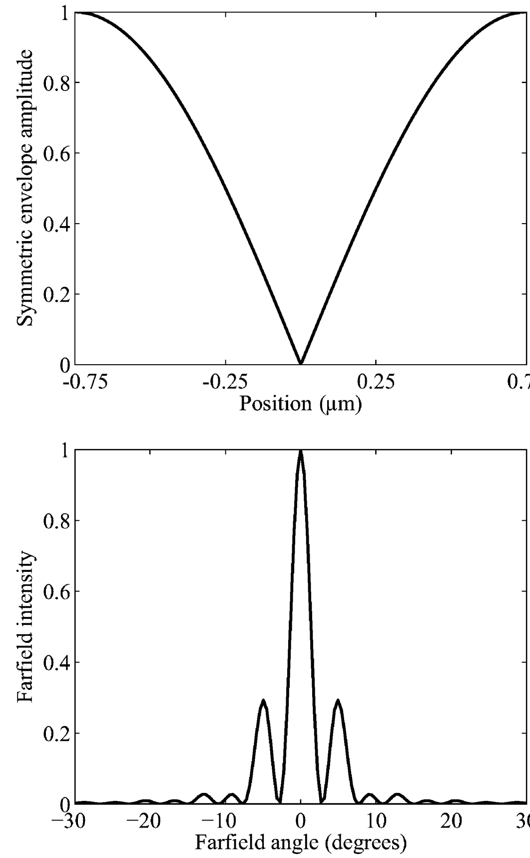

Fig. 17. Amplitude $B^s(z)$ of the symmetric component of the lasing mode and the far-field intensity pattern are plotted for a device with a π phase shift in the center of the device. The device length is 1.5 mm and $\sigma = 0.6$. The phase shift produces a single-lobe far-field pattern.

the effect of propagating each plane wave in the Floquet–Bloch expansions of the symmetric and antisymmetric modes by a length $\Lambda/2$. This produces a sign change for the odd-order plane waves in the Floquet–Bloch expansion but has no effect on the even-order plane waves.

In our calculations, the π phase shift is included by assuming a sign change for the slowly varying amplitudes, $B^s(z)$ and $B^a(z)$, at the location of the phase shift. Such a procedure is strictly valid if the Floquet–Bloch expansion consists of only the first-order plane waves (or just the odd-order plane waves). Fig. 16 compares the energy in the first-order plane wave components with remaining components for the symmetric and antisymmetric modes underneath a metal tooth. For the antisymmetric mode, the energy in the ± 1 components is much larger than the energy in the remaining plane wave components. This is not the case in the symmetric mode, where components other than ± 1 carry a significant amount of energy. Therefore, our approximation of assuming a sign change for the slowly varying amplitudes at the location of the phase shift is valid at the center of the device where the lasing mode is entirely antisymmetric (see Fig. 5).

The nearfield and far-field patterns of a device with a π phase shift are shown in Fig. 17. In the presence of the phase shift, the symmetric component of the field has the same sign on both ends of the device. Consequently, the radiated component is in phase throughout the length of the device. Radiation from both halves of the device add constructively in the surface normal direction producing a single main lobe in the far-field. The far-field radiation pattern is characterized by a central lobe that has a full-width at half-maximum (FWHM) less than 2.8 degrees wide and contains 62% of the total radiated power. The remainder of the radiated power is distributed in the higher order lobes. The energy in the higher order lobes is due to the null in the radiation in the center of the nearfield pattern, and sharp termination of the radiated field at the device edges [28].

VI. Conclusion

We have analyzed surface-emitting quantum-cascade lasers at $\lambda = 100$ μm using a scheme based upon Floquet–Bloch expansion and coupled-mode theory using PML boundary conditions for the radiation field. Our analysis is valid for the strong index contrast characteristic of second-order metal gratings. Simulations show a strong dependence of device performance upon the grating duty cycle and the laser length. Careful design allows for radiative high efficiency and low threshold gain. A π phase shift in the center of the grating can be used to transform the antisymmetric nearfield pattern into one which is symmetric along the length of the device resulting in a single-lobed far-field beam pattern.

APPENDIX I
CONNECTION WITH THE CONVENTIONAL COUPLED-MODE THEORY

Equation (8) can also be rewritten in a way that resembles the conventional couple-mode theory with slowly varying amplitudes for forward- and backward-propagating plane waves [29]

$$H(x,z) = B^{+}(z)\left[\frac{H^{s}(x,z)+H^{a}(x,z)}{2}\right] + B^{-}(z)\left[\frac{H^{s}(x,z)-H^{a}(x,z)}{2}\right]. \quad (22)$$

It must be emphasized here that the analogy with forward- and backward-going plane waves of the conventional coupled-mode theory is only approximate since the superpositions $(H^{s}+H^{a})$ and $(H^{s}-H^{a})$ contain nonnegligible backward- and forward-going plane wave components, respectively. Nevertheless, as show below, the resulting coupled-mode theory looks identical to the conventional coupled-mode theory. Plugging the expansion in (22) in (2) and using (5), (6), and (7), B^{+} and B^{-} are found to satisfy the coupled-mode equation

$$\frac{\partial}{\partial z}\begin{bmatrix} B^{+}(z) \\ B^{-}(z) \end{bmatrix} = \begin{bmatrix} i\zeta & i\kappa \\ -i\kappa & -i\zeta \end{bmatrix}\begin{bmatrix} B^{+}(z) \\ B^{-}(z) \end{bmatrix}. \quad (23)$$

With $z=0$ in the center of the device, the boundary condition for B^{+} and B^{-} at the two facets in this formulation becomes,.

$$B^{+}\left(-\frac{L}{2}\right) = B^{-}\left(-\frac{L}{2}\right) \quad (24)$$

$$B^{+}\left(\frac{L}{2}\right) = B^{-}\left(\frac{L}{2}\right) \quad (25)$$

which is equivalent to (13).

REFERENCES

[1] R. Miles, P. Harrison, and D. Lippens, Eds., *Terahertz Sources and Systems*. ser. NATO Science Series II. Dordrecht, Germany: Kluwer, 2001, vol. 27.

[2] P. Han, G. Cho, and X. Zhang, "Time-domain transillumination of biological tissue with Terahertz pulses," *Opt. Lett.*, vol. 25, pp. 242–244, Feb. 2000.

[3] D. Mittleman, R. Jacobsen, and M. Nuss, "T-ray imaging," *IEEE J. Sel. Topics Quantum Electron.*, vol. 2, no. 3, pp. 679–692, Sep./Oct. 1996.

[4] D. Mittleman, S. Hunsche, L. Boivin, and M. Nuss, "T-ray tomography," *Opt. Lett.*, vol. 22, pp. 904–906, Jun. 1997.

[5] T. Löffler, T. Bauer, K. Siebert, H. Roskos, A. Fitzgerald, and S. Cazasch, "Terahertz dark-field imaging of biomedical tissue," *Opt. Exp.*, vol. 9, pp. 616–621, Dec. 2001.

[6] B. Hu and M. Nuss, "Imaging with Terahertz waves," *Opt. Lett.*, vol. 20, pp. 1716–1718, Aug. 1995.

[7] R. Jacobsen, D. Mittleman, and M. Nuss, "Chemical recognition of gases and gas mixtures with Terahertz waves," *Opt. Lett.*, vol. 21, pp. 2011–2013, Dec. 1996.

[8] R. Köhler, A. Tredicucci, F. Beltram, H. Beere, E. Linfield, A. Davies, D. Ritchie, and F. Rossi, "Terahertz semiconductor-heterostructure laser," *Nature*, vol. 417, pp. 156–159, May 2002.

[9] B. Williams, H. Callebaut, S. Kumar, and Q. Hu, "3.4 THz quantum-cascade laser based on longitudinal-optical-phonon scattering for depopulation," *Appl. Phys. Lett.*, vol. 82, pp. 1015–1017, Feb. 2003.

[10] B. Williams, S. Kumar, H. Callebaut, Q. Hu, and J. Reno, "3.4 THz quantum-cascade laser operating above liquid nitrogen temperature," *Electron. Lett.*, vol. 39, no. 12, pp. 915–916, Jun. 2003.

[11] S. Barbieri, J. Alton, S. Dhillon, H. Beere, M. Evans, E. Linfield, A. Davies, D. Ritchie, R. Köhler, A. Tredicucci, and F. Beltram, "Continuous-wave operation of Terahertz quantum-cascade lasers," *IEEE J. Quantum Electron.*, vol. 39, no. 4, pp. 586–591, Apr. 2003.

[12] L. Ajili, G. Scalari, J. Faist, H. Beere, E. Linfield, D. Ritchie, and G. Davies, "High power quantum-cascade lasers operating at $\lambda \approx 87$ and 130 μm," *Appl. Phys. Lett.*, vol. 85, pp. 3986–3988, Nov. 2004.

[13] B. Williams, S. Kumar, H. Callebaut, and Q. Hu, "Terahertz quantum-cascade laser at $\lambda \approx 100$ μm using metal waveguide for mode confinement," *Appl. Phys. Lett.*, vol. 83, pp. 2124–2126, Sep. 2003.

[14] ——, "Terahertz quantum-cascade laser operating up to 137 K," *Appl. Phys. Lett.*, vol. 83, pp. 5142–5144, Dec. 2003.

[15] S. Kumar, B. Williams, S. Kohen, Q. Hu, and J. Reno, "Continuous-wave operation of terahertz quantum-cascade lasers above liquid-nitrogen temperature," *Appl. Phys. Lett.*, vol. 84, pp. 2494–2496, Apr. 2004.

[16] B. Williams, S. Kumar, Q. Hu, and J. Reno, "Resonant-phonon terahertz quantum-cascade laser operating at 2.1 THz ($\lambda \simeq 141$ μm)," *Electron. Lett.*, vol. 40, no. 7, Apr. 2004.

[17] S. Kohen, B. Williams, and Q. Hu, "Electromagnetic modeling of terahertz quantum-cascade laser waveguides and resonators," *J. Appl. Phys.*, vol. 97, pp. 053106–1–9, 2005.

[18] D. Hofstetter, J. Faist, M. Beck, and U. Oesterle, "Surface-emitting 10.1 μm quantum-cascade distributed feedback lasers," *Appl. Phys. Lett.*, vol. 75, pp. 3769–3771, Dec. 1999.

[19] C. Pflügel, M. Austerer, W. Schrenk, S. Golka, G. Strasser, R. Green, L. Wilson, J. Cockburn, A. Krysa, and J. Roberts, "Single-mode surface-emitting quantum-cascade lasers," *Appl. Phys. Lett.*, vol. 86, pp. 86–88, May 2005.

[20] W. Schrenk, N. Finger, S. Gianordoli, L. Hvozdara, G. Strasser, and E. Gornik, "Surface-emitting distributed feedback quantum-cascade lasers," *Appl. Phys. Lett.*, vol. 77, pp. 2086–2088, Oct. 2000.

[21] S. Li, G. Witjaksono, S. Macomber, and D. Botez, "Analysis of surface-emitting second-order distributed feedback lasers with central grating phase shift," *IEEE J. Sel. Topics Quantum Electron.*, vol. 9, no. 5, pp. 1153–1165, Sep./Oct. 2003.

[22] G. Witjaksono and D. Botez, "Surface-emitting, single-lobe operation from second-order distributed-reflector lasers with central grating phase shift," *Appl. Phys. Lett.*, vol. 78, pp. 4088–4100, Jun. 2001.

[23] G. Witjaksono, S. Li, J. Lee, D. Botez, and W. Chan, "Single-lobe, surface-normal beam surface emission from second-order distributed feedback lasers with half-wave grating phase shift," *Appl. Phys. Lett.*, vol. 83, pp. 5365–5367, Dec. 2003.

[24] N. Finger, W. Schrenk, and E. Gornik, "Analysis of TM-polarized DFB laser structures with metal surface gratings," *IEEE J. Quantum Electron.*, vol. 36, no. 7, pp. 780–786, Jul. 2000.

[25] P. Ho and Y. Lu, "A mode-preserving perfectly matched layer for optical waveguides," *IEEE Photon. Technol. Lett.*, vol. 15, no. 9, pp. 1234–1236, Sep. 2003.

[26] N. Ashcroft and N. Mermin, *Solid State Physics*. New York: Holt, Rinehart, and Winston, 1976.

[27] S. Chuang, *Physics of Optoelectronic Devices*. New York: Wiley, 1995.

[28] R. Noll and S. Macomber, "Analysis of grating surface-emitting lasers," *IEEE J. Quantum Electron.*, vol. 26, no. 3, pp. 456–466, Mar. 1990.

[29] H. Kogelnik and C. Shank, "Coupled-wave theory of distributed feedback lasers," *J. Appl. Phys.*, vol. 43, pp. 2327–2335, May 1972.

[30] D. Staelin, A. Morgenthaler, and J. Kong, *Electromagnetic Waves*. Englewood Cliffs, NJ: Prentice Hall, 1994.

Martin Schubert (S'04) was born in 1982 in Stuttgart, Germany. He received the B.S. and M.Eng. degrees in electrical engineering from Cornell University, Ithaca, NY, in 2004 and 2005, respectively, where he is currently working toward the Ph.D. degree in electrical engineering.

His current research focuses on semiconductor optoelectronics.

Farhan Rana (M'03) was born in 1971 in Karachi, Pakistan. He received the B.S., M.S., and Ph.D. degrees, all in electrical engineering, from the Massachusetts Institute of Technology (MIT), Cambridge.

He worked on a variety of different topics related to semiconductor optoelectronics, quantum optics, and mesoscopic physics during his Ph.D. research. Before starting his doctoral studies, he worked at IBM's T. J. Watson Research Center, Yorktown Heights, NY, on silicon nanocrystal and quantum dot memory devices. After finishing his doctoral work in 2002, he joined the faculty of Electrical and Computer Engineering, Cornell University, Ithaca, NY.

Dr. Rana was awarded the U.S. National Science Foundation Faculty CAREER Award in 2004. His current research focuses on semiconductor optoelectronics and quantum optics.